(Preprint) AAS 19-032

LIDAR-GENERATED DIGITAL ELEVATION MODELS FOR HAZARD DETECTION - REQUIREMENTS AND ANALYSIS

Po-Ting Chen[*], Siddarth Kaki[†], A. Miguel San Martin[‡], David Skulsky[§], Anup Katake[¶] and Nikolas Trawny[‖]

Jet Propulsion Laboratory, California Institute of Technology, 4800 Oak Grove Dr., Pasadena, CA 91109, USA

Hazard detection is an enabling technology for safe landing on planetary bodies with limited terrain knowledge, such as Jupiter's icy moon Europa. Using a Light Detection and Ranging (LIDAR) sensor, a lander scans the landing site and constructs a Digital Elevation Model (DEM) in real-time during descent. This DEM is processed by hazard detection algorithms to construct a safety cost map and determine the safest landing location. The target location is then provided to the guidance and control system to execute a hazard avoidance divert maneuver. We derived requirements on the DEM quality and accuracy from the proposed Europa Lander Deorbit, Descent, and Landing (DDL) concept of operations and the lander hazard tolerance. A modular geometric LIDAR modeling tool and re-gridding algorithms were developed and integrated into a high-fidelity 6-DOF dynamics simulation. The modular nature of the model allows us to simulate various detector aspect ratios, laser pulse repetition rates, scan mechanisms, optical designs, and basic error models. This tool was developed to support the parametric sensitivity analysis of the DEM quality with respect to the LIDAR design, site topography, scanning pattern, noise properties, and navigation state knowledge errors, and to evaluate the generated DEMs against the Europa Lander requirements.

INTRODUCTION

Europa is the smallest moon of Jupiter and is one of a few locations within the Solar System that is thought to be capable of supporting life in the present day. It is hypothesized that there exists a large liquid water ocean underneath its crust. Given this possibility the science community is intensely interested in exploring Europa and characterizing its surface and subsurface composition. Since the terrain knowledge of Europa is limited, a safe and successful landing requires the lander vehicle to construct a terrain model of the intended landing location and identify potential hazards in real-time as it descends from orbital altitude.

The Europa Lander Deorbit, Descent, and Landing mission concept has been presented in past conferences.[1,2] The following is a brief description of the concept of operations for the hazard detection phase. It starts at approximately 1 km altitude, where the lander would maneuver to align

[*]Member of Technical Staff, Guidance and Control Section, MS 198-326.
[†]Dept. of Aerospace Engineering and Engineering Mechanics, The University of Texas at Austin.
[‡]Engineering Fellow, Guidance and Control Section, MS 198-326.
[§]Principal Member of Technical Staff, Guidance and Control Section, MS 321-560.
[¶]Member of Technical Staff, Guidance and Control Section, MS 198-235.
[‖]Member of Technical Staff, Guidance and Control Section, MS 198-326.

itself above the intended landing location using thrusters. After the precision landing maneuver, it maintains a -23 m/s constant vertical descent velocity as it approaches the surface. At 500 m altitude, the model construction phase is initialized by imaging the surface and generating a 100 m $\times 100$ m Digital Elevation Model (DEM) centered about the intended landing location. The time allotted for DEM construction is 2 s. The on-board hazard detection algorithm then processes the DEM to form a safety map for landing location selection. This landing location is then transmitted to the Guidance, Navigation and Control (GNC) system to steer the lander to a safe landing.

There are several different approaches for hazard detection, such as a optical monocular camera, stereo cameras, radar, and Light Detection and Ranging (LIDAR) sensor. Out of all these approaches, the LIDAR-based system was determined to be the most suitable solution for landing on Europa.[1,2] The advantages of a LIDAR-based approach include high-resolution images, fast data acquisition rate, and robustness against changes in natural illumination. However, due to the size of the required mapped region, map resolution, and time allotment, a scanning-based LIDAR system is necessary for this mission. As a result, the hazard detection system processes a DEM created by stitching multiple images together. The quality of the DEM is affected by several factors including system sizing, vehicle motion, scanning pattern, and ground terrain. Therefore, it is essential to simulate the range measurements and investigate the coverage and the accuracy of the estimated DEM based on these factors. While there exists several LIDAR simulation software,[3,4] they are not directly applicable to the Europa Lander mission concept. This work is the beginning of an extensive sensitivity analysis laid out to support the development of the GNC system of the Europa Lander concept.

This paper describes a C++ based LIDAR simulation tool for DEM generation. The modular nature of the model allows one to vary the detector array specifications, interchange different scan mechanisms, and adjust the scanning patterns. Additional LIDAR components can be programmed into this software to form a component library for other future missions. The LIDAR model is integrated with a dynamics simulator, which allows the user to simulate LIDAR measurements on a moving platform both in space and on the ground. The measurements and the resulting DEM depend on the lander trajectories and are affected by several error sources. A specialized post-processing program was developed to evaluate the coverage and the accuracy of the estimated DEM.

MODEL DESCRIPTION

The LIDAR simulation software leverages the architecture of DSENDS, which is a software environment for high-fidelity 6 Degrees-of-Freedom (DOF) multi-body simulation.[5] The LIDAR model was developed as a software module, so it can be integrated into the DSENDS simulation environment. The user initializes the LIDAR model by providing a list of system parameters. These include LIDAR-specific parameters, noise model parameters, and navigation error model parameters. The LIDAR-specific parameters include number of detector pixels, field-of-view, number of anti-aliasing sub-pixels (range measurement of one pixel is a sample average of multiple sub-pixels), DEM resolution, laser pulse repetition rate, scanning time, scanning mechanism, and scanning pattern. The noise model parameters include range noise variance, range bias, dead-pixel percentage, and pixel dropout percentage. The dead-pixel percentage accounts for complete detector pixel failure, whereas the pixel dropout percentage accounts for random measurement dropout due to intermittent radiation effects. The navigation error model parameters include position bias, velocity bias, orientation bias, and angular rate bias. Figure 1 is a block diagram showing the individual components of the LIDAR model.

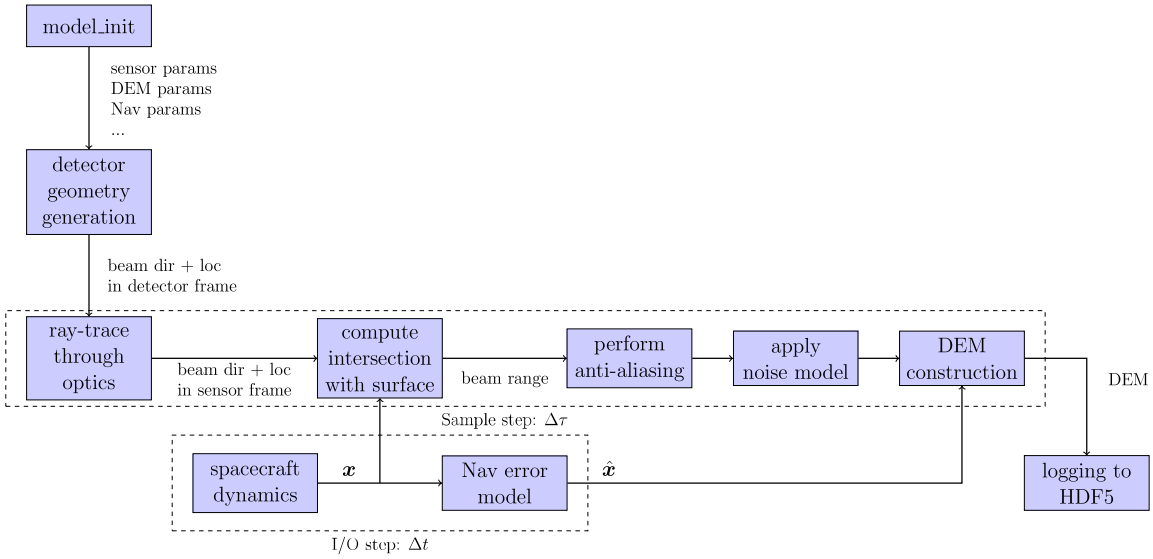

Figure 1. Block diagram of the components of the LIDAR simulation.

LIDAR Modeling

Following the model initialization step is the detector geometry generation step. A perspective detector model is constructed by specifying the detector field-of-view, the number of pixels, and the distribution of the pixels. The measurement associated with each pixel is obtained by ray-tracing technique. The ray originates from the focal point, then it goes through the pixel center before it is redirected by the scanning mechanism such that it leaves the LIDAR output frame along a particular direction. In addition to the flash LIDAR model, two different scanning mechanisms have been implemented, namely the Risley prism and the Fast-Steering-Mirror (FSM). The scanning profile of each system can be decomposed into 2 DOF, and the time evolution of each DOF is modeled as a function of time. Additional details regarding the modeling of these scanning mechanism can be found in various publications.[6–8] The true range value, r, from the LIDAR output frame to the ground terrain is obtained using built-in DSENDS function for ray-intersection with a topographic object. Following the ray-intersection calculation, the true range value is corrupted according to the specified measurement noise parameters.

The coordinate system of the LIDAR model is shown in Figure 2. The D frame represents the DEM frame; the B frame is the lander body frame; and the L frame is the LIDAR frame. From the figure, the vector from the LIDAR frame origin to a point on the ground is

$$^{L}\boldsymbol{y} = {}^{L}\boldsymbol{n}\,[r + b + v] + {}^{L}\boldsymbol{b}, \tag{1}$$

where $^{L}\boldsymbol{b}$ is the offset between the LIDAR origin and the output of a light ray expressed in the LIDAR frame; $^{L}\boldsymbol{n}$ is the direction of the ray at a particular time expressed in the LIDAR frame; and r is the range to the ground along $^{L}\boldsymbol{n}$. The time evolution of $^{L}\boldsymbol{n}$ depends on the scanning mechanism. The measurement noise, v, is modeled as white Gaussian noise and b is a constant range bias.

In order to construct the DEM, $^{L}\boldsymbol{y}$ has to be transformed from the LIDAR frame to the DEM frame using the lander position and the lander orientation with respect to the DEM frame. Let $^{D}\boldsymbol{s}$

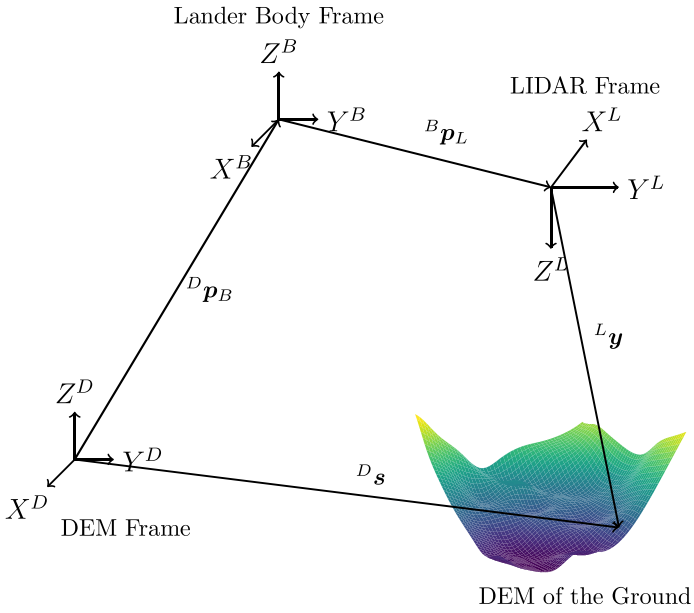

Figure 2. Frame definitions

be the position vector of a point in the DEM frame, then the relationship between ${}^L\boldsymbol{y}$ and ${}^D\boldsymbol{s}$ is

$$\begin{bmatrix} {}^D\boldsymbol{s} \\ 1 \end{bmatrix} = \underbrace{\begin{bmatrix} {}^D_L R & {}^D\boldsymbol{p}_L \\ 0 & 1 \end{bmatrix}}_{{}^D_L H} \begin{bmatrix} {}^L\boldsymbol{y} \\ 1 \end{bmatrix}, \tag{2}$$

where ${}^D_L R$ is the rotation from the LIDAR frame to the DEM frame and ${}^D\boldsymbol{p}_L$ is the location of the LIDAR frame origin expressed in the DEM frame. This homogeneous transformation can be further decomposed as

$${}^D_L H = \underbrace{\begin{bmatrix} {}^D_B R & {}^D\boldsymbol{p}_B \\ 0 & 1 \end{bmatrix}}_{{}^D_B H} \underbrace{\begin{bmatrix} {}^B_L R & {}^B\boldsymbol{p}_L \\ 0 & 1 \end{bmatrix}}_{{}^B_L H}, \tag{3}$$

where ${}^D_B H$ and ${}^B_L H$ represent the homogeneous transformations between the DEM, the body and the LIDAR frames.

Navigation Error Model

The transformation shown in Eq. (3) is an ideal equation, which is only valid if one has access to the true lander position, ${}^D\boldsymbol{p}_B$, and orientation, ${}^D_B R$. In practice, only the estimates,

$$\begin{aligned} {}^D\hat{\boldsymbol{p}}_B &= {}^D\boldsymbol{p}_B - {}^D\tilde{\boldsymbol{p}} \\ {}^D_B\hat{R} &= {}^D_B R\tilde{R}(\tilde{\boldsymbol{\theta}}), \end{aligned} \tag{4}$$

are available, where ${}^D\tilde{\boldsymbol{p}}$ is the position error and $\tilde{\boldsymbol{\theta}}$ is the orientation error expressed in roll, pitch and yaw angles. Substituting these estimates for the true values in ${}^D_B H$ gives

$${}^D_L\hat{H} = \begin{bmatrix} {}^D_B R\tilde{R}(\tilde{\boldsymbol{\theta}}) & {}^D\boldsymbol{p}_B - {}^D\tilde{\boldsymbol{p}} \\ 0 & 1 \end{bmatrix} \begin{bmatrix} {}^B_L R & {}^B\boldsymbol{p}_L \\ 0 & 1 \end{bmatrix}. \tag{5}$$

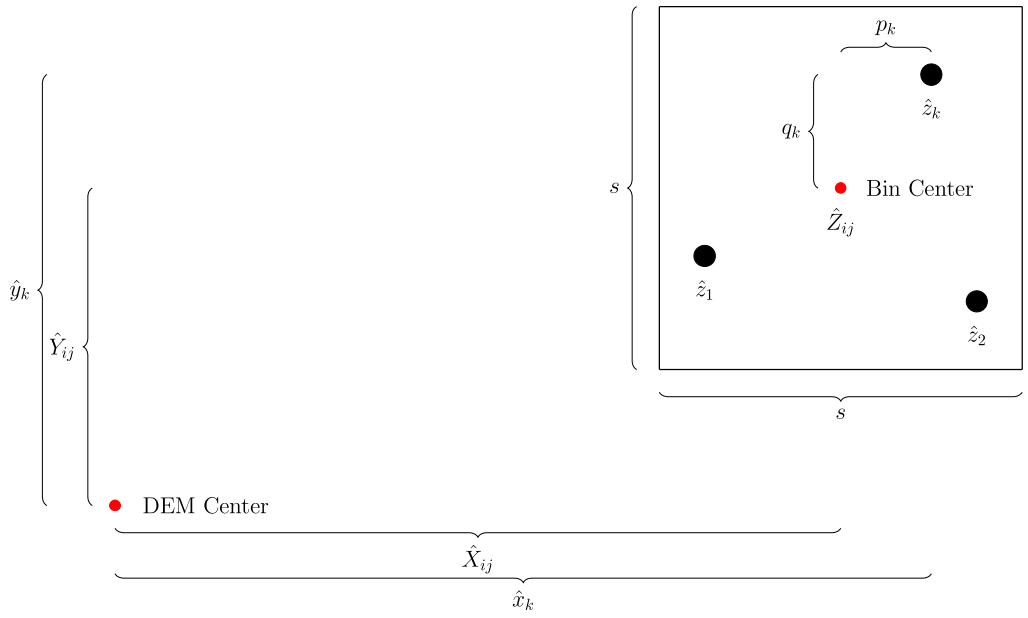

Figure 3. Coordinate systems for the DEM weighted average.

The time evolutions of these errors are modeled as

$$\begin{aligned} {}^{D}\tilde{\boldsymbol{p}} &= \boldsymbol{a}_p + \boldsymbol{a}_v(t - t_0) \\ \tilde{\boldsymbol{\theta}} &= \boldsymbol{a}_\theta + \boldsymbol{a}_\omega(t - t_0), \end{aligned} \tag{6}$$

where $\boldsymbol{a}_p$, $\boldsymbol{a}_v$, $\boldsymbol{a}_\theta$, and $\boldsymbol{a}_\omega$ are user-specified error parameters. An alternative method is to use stochastic processes to model the navigation errors. This option was not used because the LIDAR scanning time for the Europa Lander mission concept is short relative to the random walk behavior of the position estimate. Thus, the dominant error source is the initial condition uncertainty. Replacing the true homogeneous transformation in Eq. (2) with the estimated transformation gives

$$\begin{bmatrix} {}^{D}\hat{\boldsymbol{s}} \\ 1 \end{bmatrix} = {}^{D}_{L}\hat{H} \begin{bmatrix} {}^{L}\boldsymbol{y} \\ 1 \end{bmatrix}. \tag{7}$$

The estimated DEM is constructed using ${}^{D}\hat{\boldsymbol{s}}$.

DEM Construction

The first step in DEM construction is creating a regularly partitioned rectangular mesh centered at the DEM frame origin. Each intersection of the mesh grid defines the center of a bin whose resolution, s, is specified by the user in the initialization step. The coordinates of the bin center are denoted by $\hat{X}_{ij}$ and $\hat{Y}_{ij}$. Let the true and the estimated coordinates of the position vector from a single LIDAR measurement be denoted by

$${}^{D}\boldsymbol{s} = \begin{bmatrix} x \\ y \\ z \end{bmatrix}, \quad \text{and} \quad {}^{D}\hat{\boldsymbol{s}} = \begin{bmatrix} \hat{x} \\ \hat{y} \\ \hat{z} \end{bmatrix}. \tag{8}$$

The estimated Z coordinate, $\hat{z}$, is sorted into a single bin based on the values of $\hat{x}$ and $\hat{y}$.

Table 1. DEM Quality Metrics

Mapped region coverage	The number of invalid pixels cannot exceed 1% of the mapped region.
Hole size	Following the 8-connected rule, the number of connected invalid pixels cannot exceed 10 pixels.
Distance to the nearest valid pixel	The maximum distance from an invalid pixel to the nearest valid pixel cannot exceed 1 pixel.
Relative elevation error	The elevation error of all valid pixels over the lander footprint shall not exceed 5 cm (95%ile) over the entire mapped region.
Relative horizontal error	The horizontal error of all valid pixels over the lander footprint shall not exceed 5 cm (95%ile) over the entire mapped region.
Absolute horizontal error	The mean horizontal error over a lander footprint shall not exceed 1 m for 95% of the entire map.

After the sorting step, the elevation value of the ij^{th} bin is the weighted average of all the estimated elevation coordinates, $\hat{z}_k$, in the bin, where k denotes the measurement index within a bin. See Figure 3.

$$\hat{Z}_{ij} = \sum_{k=1}^{N} w_k \hat{z}_k, \quad w_k = \frac{\breve{w}_k}{\sum_{k=1}^{N} \breve{w}_k}. \tag{9}$$

The unnormalized weight is $\breve{w}_k = (1-q_k)(1-p_k)$, where the values of p_k and q_k are the X and the Y distances of the k^{th} measurement to the bin center respectively. From the definition of Eq. (9), the elevation value of a particular bin is non-zero if the bin contains at least one measurement. If the bin is empty, then $\hat{Z}_{ij}$ is set to invalid (NaN). This construction method is a modified version of the bilinear interpolation method.[9] Specifically, it does not use the value of neighboring bins for interpolation. This is a more conservative approach. Furthermore, it does not use *a priori* information about the terrain, which is suitable for the Europa Lander mission concept because there is limited information about the surface.

The true elevation value of the ij^{th} bin is $Z_{ij} = H(X_{ij}, Y_{ij})$, where X_{ij} and Y_{ij} are the true X and Y coordinates of the bin center. The function $H(\cdot\,,\cdot)$ represents the true DEM. The true X_{ij} and Y_{ij} coordinates are obtained using the true range, r, and the ideal transformation in Eq. (3). All 6 coordinates, $\hat{X}_{ij}$, $\hat{Y}_{ij}$, $\hat{Z}_{ij}$, X_{ij}, Y_{ij}, and Z_{ij} are saved to disk for DEM quality evaluation.

DEM EVALUATION TOOL

The DEM evaluation step considers two categories: coverage and accuracy. The required mapped region is defined as a circular area with a radius of 50 m and centered about the intended landing location. Three metrics are used to evaluate the DEM coverage quality. The first metric is the number of invalid pixels in the required mapped region. The second metric considers the size of the invalid pixel grouping following the 8-connected rule. This rule considers the immediate neighboring pixels: $(i+1, j+1)$, $(i+1, j)$, $(i+1, j-1)$, $(i, j-1)$, $(i-1, j-1)$, $(i-1, j)$, $(i-1, j+1)$, and $(i, j+1)$. The third metric considers the distance between the invalid pixel and

the closest valid pixel. For the accuracy category, there are also three metrics, namely the absolute horizontal error, relative elevation error and relative horizontal error with respect to the true ground terrain. Since the main purpose for constructing the DEM is for hazard detection, the accuracy of the DEM is evaluated with the consideration of the lander footprint. Table 1 is a summary of the DEM quality metrics for the hazard detection phase of the Europa Lander concept.

The absolute coordinate errors are defined as

$$e_{X,ij} = X_{ij} - \hat{X}_{ij}, \quad e_{Y,ij} = Y_{ij} - \hat{Y}_{ij}, \quad e_{Z,ij} = Z_{ij} - \hat{Z}_{ij}. \tag{10}$$

Assuming the lander is centered at the ij^{th} bin, then the absolute error metrics used by the evaluation tool are

$$\breve{e}_{X,ij} = mean(e_{X,lk}), \quad \breve{e}_{Y,ij} = mean(e_{Y,lk}), \quad \breve{e}_{Z,ij} = mean(e_{Z,lk}), \tag{11}$$

where the indices l and k iterate over all the pixels under the lander footprint. These values are used to determine the local position bias over an individual lander footprint. The relative errors over an individual lander footprint are

$$\tilde{e}_{X,ij} = Q_q(|e_{X,lk} - \breve{e}_{X,ij}|), \quad \tilde{e}_{Y,ij} = Q_q(|e_{Y,lk} - \breve{e}_{Y,ij}|), \quad \tilde{e}_{Z,ij} = Q_q(|e_{Z,lk} - \breve{e}_{Z,ij}|), \tag{12}$$

where $Q_q(\cdot)$ is the q^{th} percentile of the argument. These values are used to assess the local variations within a lander footprint.

SIMULATION RESULTS

The DSENDS software and the LIDAR model can be programmed to simulate various lander trajectories and LIDAR model parameters. For illustration purposes, the following are samples of the estimated DEM and the evaluation results. The reference trajectory for the simulation is a vertical descent on Europa from an altitude of 500 m and an initial vertical velocity of -23 m/s. The LIDAR system parameters used in the following examples do not reflect the actual LIDAR system parameters for the Europa Lander mission concept. In the following simulations, the scanning time is 2 s with a sample frequency of 20 kHz. The scanning mechanism is an FSM following a line search pattern starting from the upper left-hand corner. The detector consists of 18×18 pixels. The ground sample distance between 2 pixels at 500 m altitude is 4.44 cm, and the DEM resolution is 5 cm. The lander footprint used for the evaluation is 1.7 m $\times$ 1.7 m.

Example 1

In the first example, we show the accuracy of the DEM when there are no measurement noises or navigation errors. The true and estimated DEM in this simulation are shown in Figure 4. The true DEM is a flat surface with 10 right circular cones distributed around the origin. Each cone has a height of 10 m and base radius of 3 m. The estimated DEM is constructed using Eq. (9) and multiple LIDAR scans. Because there is sufficient overlap between scans, there are no large holes in the estimated DEM. Overall it captures the shape and the location of the cones.

The difference between the true DEM and the estimated DEM, $e_{Z,ij}$, computed using Eq. (10) is shown in Figure 5. Despite having zero measurement noise, the elevation errors can be as large as ± 10 cm. After examining the plot more closely, we found these errors are located on the cone surfaces and are caused by the quantization of the range measurements. To illustrate this point we

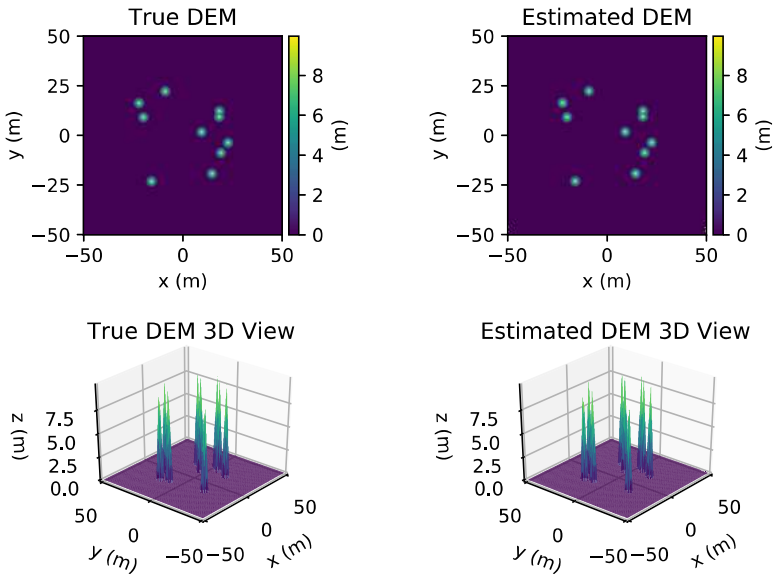

Figure 4. True and estimated DEM for example 1.

show the worst case quantization errors along the X, the Y, and the 45° diagonal directions of a right circular cone. They are

$$e_x = \frac{\partial z}{\partial x}\frac{s}{2}, \quad e_y = \frac{\partial z}{\partial y}\frac{s}{2}, \quad e_d = \frac{1}{\sqrt{2}}\left(\frac{\partial z}{\partial x} + \frac{\partial z}{\partial y}\right)\frac{\sqrt{s^2+s^2}}{2} = \frac{s}{2}\left(\frac{\partial z}{\partial x} + \frac{\partial z}{\partial y}\right), \tag{13}$$

where s is the DEM resolution. Evaluating Eq. (13) at a radial distance (< 3 m) away from the cone center gives $e_x = e_y = 8.3$ cm and $e_d = 11.8$ cm. These values illustrate the impact of elevation change on the DEM accuracy. Because of the quantization errors, 1681 pixels out of a total of 3,141,521 pixels do not satisfy the 95%ile relative elevation error requirement. From the form of Eq. (13), one can mitigate the effect of quantization error by choosing a target area with low elevation variation or increasing the DEM resolution. If both options are not feasible, then an alternative solution is to leverage the DEM construction process. Since the elevation value of the ij^{th} bin is a weighted average of multiple range measurements, it is possible to use multiple LIDAR scans of the same area to average out the quantization errors.

Example 2

For example 2, the coverage and the accuracy evaluation results are examined more closely. The coverage evaluation plot in Figure 6 is a binary map showing the location and the percentage of invalid pixels. Next to that is a binary map showing the location of the holes that fail the maximum distance to valid pixel requirement. Below both plots is a histogram showing the number of holes vs. hole size. In Figure 7, the left portion of the accuracy evaluation plot shows the absolute errors computed using Eq. (11). The 95%ile absolute error over the entire mapped region for each axis is provided at the top of each subplot. The right portion of the same figure shows the result of Eq. (12), where $q = 95$. The number of touchdown locations that violate the 95%ile relative error requirement is shown at the top of each subplot.

In example 2, the true DEM is the same as in example 1. However, Gaussian noise was added to the range measurement. The 3σ noise value is 5 cm. The evaluation results in Figure 6 show

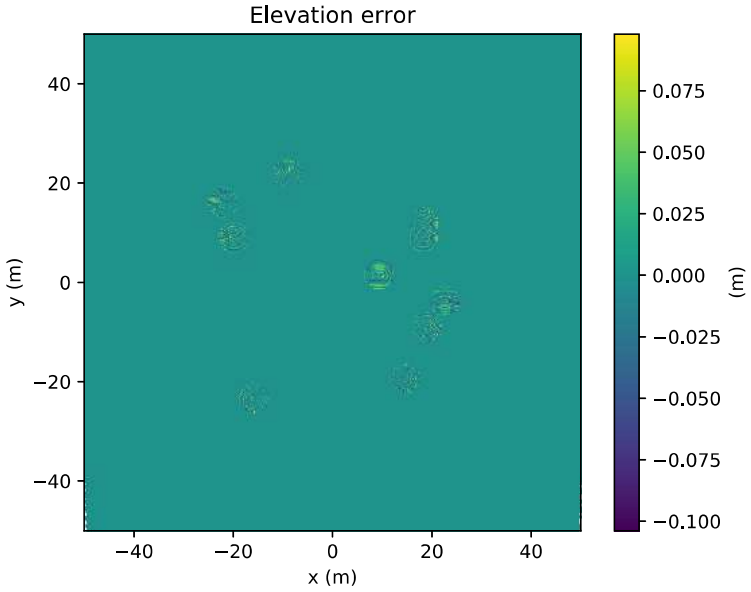

Figure 5. Absolute Z coordinate errors of example 1.

there are 13 invalid pixels within the required mapped region, and the total invalid percentage is $< 0.001\%$. All pixels satisfy the distance and the hole size requirements. Since the invalid percentage is much lower than the requirement, it may be possible to reduce the sample rate or the number of detector pixels and still satisfy the coverage requirements in this example.

Figure 7 shows the results of the accuracy evaluation. Since no navigation errors were added in the construction of the DEM, the horizontal absolute errors are in the order of millimeters. The relative horizontal errors shown in the plots are mostly due to the sorting process of the measurement. They are in the order of the DEM resolution and are concentrated along the outer region. Since the quantization error is much larger than the 2σ bound of the Gaussian range noise, the scale of the color bar for the relative elevation error is dominated by the quantization error. The quantization errors affect both the absolute and the relative elevation errors because the cone footprint is larger than the lander footprint.

Example 3

The true and the estimated DEM for the third example are shown in Figure 8. Figure 9 show the results of the accuracy evaluation. The lander trajectory and scanning pattern are the same as the previous 2 examples. The true DEM in this example was obtained by interpolating a 12.5 m resolution Europa DEM. Due to the interpolation step, the true DEM only captures the Europa terrain at large-scale. While it is possible to place geometric primitives such as hemispheres, cones, and pyramids on top of the interpolated DEM to create small-scale features, careful thought and consideration are necessary so that they are consistent with the actual Europa terrain.

In addition to the measurement noise, navigation errors were added in this example, where the velocity error vector is $\boldsymbol{a}_v = \begin{bmatrix} 0.3 & 0.3 & 0.7 \end{bmatrix}^T$ m/s. Because of this velocity bias error, the position error, ${}^D\tilde{\boldsymbol{p}}$, accumulates with time. Since the lower region of the DEM was scanned last, the absolute error in that region is the largest as shown in the left subplots of Figure 9. The absolute horizontal errors are approximately 0.6 m $= 0.3$ m/s $\times 2$ s, which is consistent with the x and y components

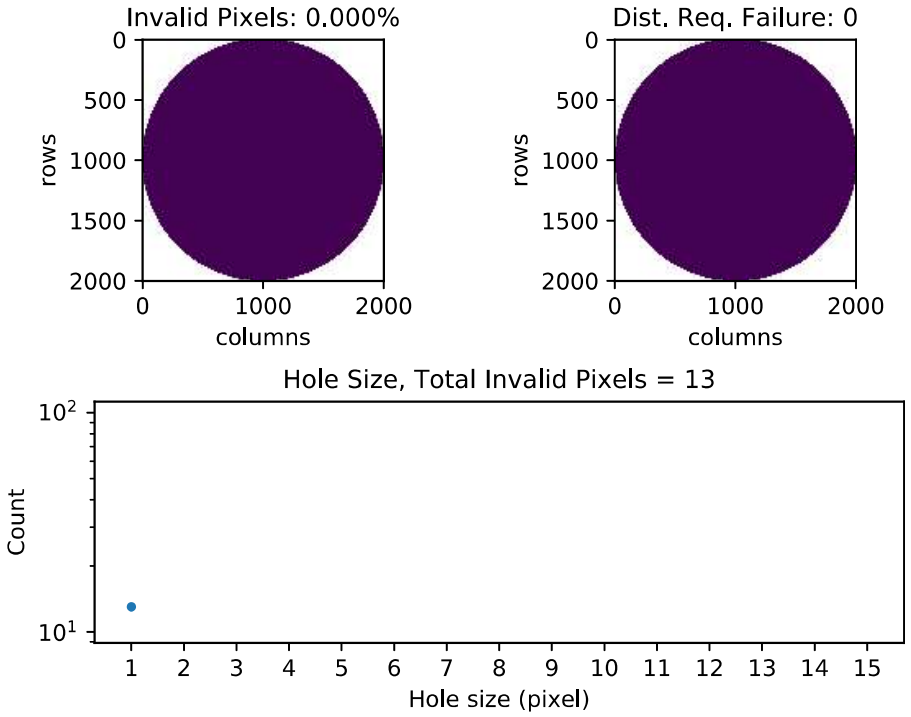

Figure 6. DEM coverage result for example 2. The two upper plots are binary maps showing the locations of invalid pixels and distance requirement failures.

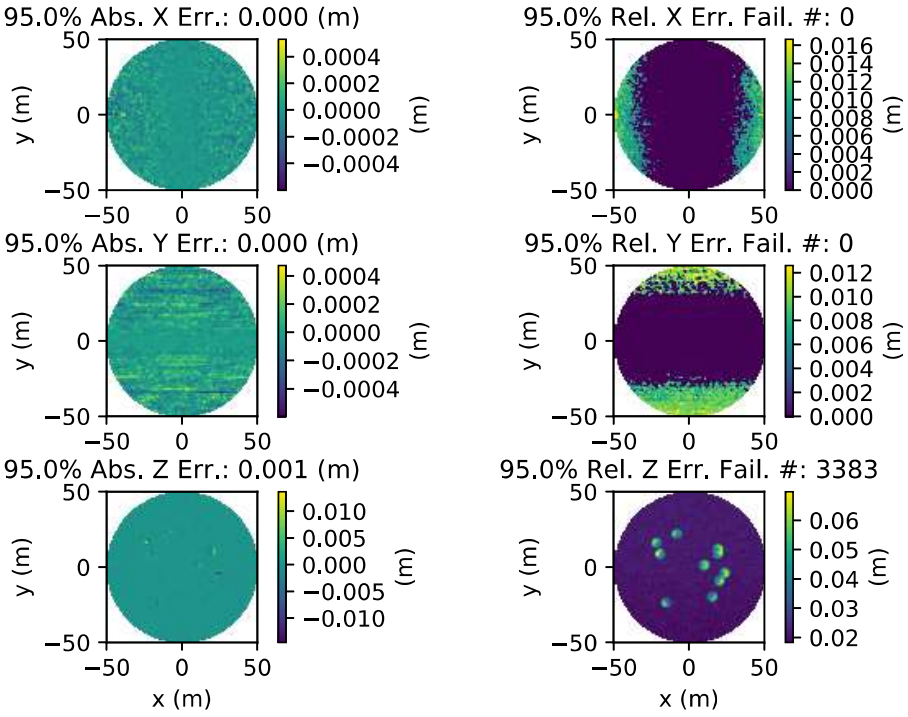

Figure 7. DEM accuracy result for example 2. The left subplots are the absolute error metrics, $\breve{e}_{ij}$, and the right subplots are the relative error metrics, $\tilde{e}_{ij}$.

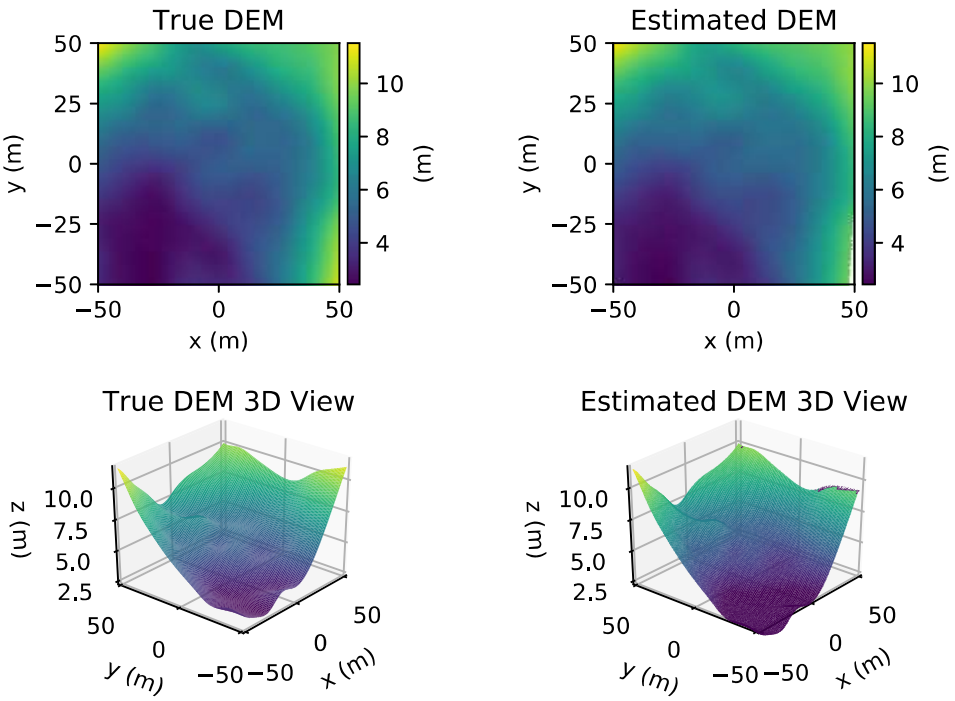

Figure 8. True and estimated DEM for example 3.

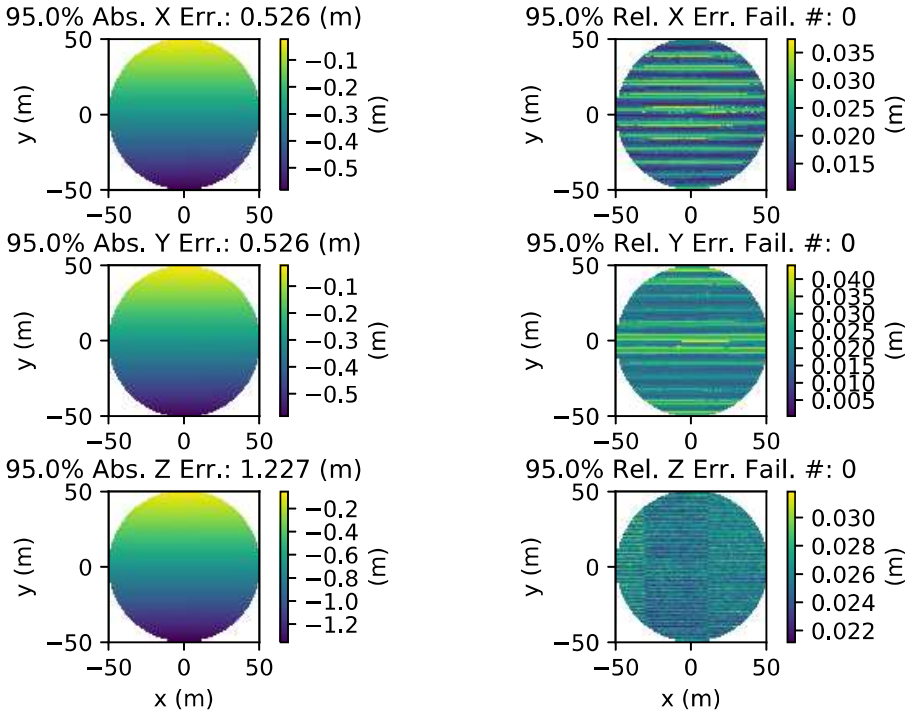

Figure 9. DEM accuracy result for example 3. The left subplots are the absolute error metrics, $\breve{e}_{ij}$, and the right subplots are the relative error metrics, $\tilde{e}_{ij}$.

of $\boldsymbol{a}_v$. Similar result can be seen in the elevation direction. The absolute elevation error is approximately $1.4\text{ m} = 0.7\text{ m/s} \times 2\text{ s}$. The majority of the navigation errors is captured by the absolute error metrics. This type of error can be mitigated by either reducing the velocity knowledge error or the LIDAR scanning time. As shown in Figure 9, all pixels satisfy the relative error requirements. The navigation errors have slight impact on the relative error metrics for this scanning pattern. The horizontal errors remain in the order of the DEM resolution, and the relative elevation errors are slightly below the range noise 2σ bound of 3.33 cm that one expects if there are no navigation errors.

CONCLUSION

In summary, this paper describes the LIDAR simulation and the DEM evaluation tools devised to facilitate the development of active hazard detection and avoidance technology. This technology is essential to future lander missions since it enables safe landing capability at locations with limited terrain knowledge. The simulation and evaluation tools allow the users to test different LIDAR configurations, ground terrain, noise parameters and lander trajectories in order to determine the most suitable combination for a particular mission. Besides adding additional interchangeable LIDAR components to the software, other future enhancements include the use of GPU to reduce computation time and the generation of a DEM uncertainty map.

ACKNOWLEDGEMENT

This research was carried out at the Jet Propulsion Laboratory, California Institute of Technology, under a contract with the National Aeronautics and Space Administration.

REFERENCES

[1] E. D. Skulsky, A. M. San Martin, D. M. Kipp, A. K. Zimmer, G. Singh, F. Serricchio, N. Trawny, A. Katake, M. Greco, and A. Frick, "Landing on Europa: Challenges, Technologies, and a Strategy," in *Proceedings of the Advances in the Astronautical Sciences Guidance, Navigation and Control 2017*, vol. 159, 2017.

[2] N. Trawny, A. Katake, Y. Cheng, D. Conway, M. San Martin, D. Skulsky, and A. E. Jonhson, "The Intelligent Landing System for Safe and Precise Landing on Europa," in *Proceedings of the Advances in the Astronautical Sciences Guidance, Navigation and Control*, vol. 159, 2017.

[3] Utah State University Space Dynamics Laboratory, *USU LADAR SIM Public Release 3.0 Users Manual, Ladar Sensor Model Development and Assessment*, March 2007.

[4] S. D. Brown, D. D. Blevins, and J. R. Schott, "Time-Gated Topographic LIDAR Scene Simulation," in *Laser Radar Technology and Applications X*, vol. 5791, pp. 342–354, International Society for Optics and Photonics, 2005.

[5] J. M. Cameron, A. Jain, P. D. Burkhart, E. S. Bailey, B. Balaram, E. Bonfiglio, M. Ivanov, J. Benito, E. Sklyanskiy, and W. Strauss, "DSENDS: Multi-mission Flight Dynamics Simulator for NASA Missions," in *AIAA SPACE 2016*, p. 5421, 2016.

[6] Y. Yang, "Analytic Solution of Free Space Optical Beam Steering Using Risley Prisms," *Journal of Lightwave Technology*, vol. 26, no. 21, pp. 3576–3583, 2008.

[7] Y. Li, "Third-Order Theory of the Risley-Prism-Based Beam Steering System," *Applied optics*, vol. 50, no. 5, pp. 679–686, 2011.

[8] J. M. Hilkert, G. Kanga, and K. Kinnear, "Line-of-Sight Kinematics and Corrections for Fast-Steering Mirrors Used in Precision Pointing and Tracking Systems," in *Airborne Intelligence, Surveillance, Reconnaissance (ISR) Systems and Applications XI*, vol. 9076, p. 90760F, International Society for Optics and Photonics, 2014.

[9] A. E. Johnson, A. R. Klumpp, J. B. Collier, and A. A. Wolf, "Lidar-Based Hazard Avoidance for Safe Landing on Mars," *Journal of Guidance, Control, and Dynamics*, vol. 25, no. 6, pp. 1091–1099, 2002.